DOI: 10.13009/EUCASS2025-404

EXPERIMENTAL CHARACTERIZATION OF A H2-FUELED DUAL-SWIRL BURNER

Fabio Cozzi, Francesca Iapaolo, Edoardo Ciuffoli and Pierfelice Rocco*
Combustion and Optical Diagnostics Lab, Department of Energy, Politecnico di Milano
Via Lambruschini 4, Milan, Italy
fabio.cozzi@polimi.it – francesca.iapaolo@polimi.it – edoardo.ciuffoli@mail.polimi.it – pierfelice.rocco@mail.polimi.it
*Corresponding author

Abstract
This study investigates flame morphology, NO_x emissions, and stability in a Rich-Premixed, Air-Staged, Hydrogen-fueled Dual-Swirl burner (RAPIDS-H). The flame consistently shows an M-shaped profile, with the central V-shaped region flattening as the premix equivalence ratio (Φ_p) increases. Flame length and NO_x emissions ($EINO_x \approx$ 1.7 - 2.8 g/kgH_2) decrease with lower global equivalence ratio (Φ_g), likely due to cooler and more compact flames. Both mild and strong flashback events are observed, but flashback can be reversed without flame extinction. Future work will aim to enhance flashback resistance and analyze flow structure and NO_x formation for performance optimization.

1. Introduction

Hydrogen is increasingly recognized as a key enabler for the deep decarbonization of hard-to-abate sectors, driven by the urgent need to mitigate climate change, comply with emerging environmental regulations, and support the global transition toward sustainable energy systems. Among the sectors where hydrogen may play a transformative role, aviation stands out due to its reliance on high specific energy carriers and the limited alternatives available for long-range flight decarbonization.
The absence of carbon in its molecular structure and its high gravimetric energy density (approximately 120 MJ/kg, nearly three times that of kerosene) make hydrogen, at least in principle, an excellent alternative to conventional fossil fuels. However, the transition to hydrogen-fuelled propulsion systems presents formidable scientific and engineering challenges. In combustion applications, hydrogen's unique physico-chemical properties diverge significantly from those of traditional hydrocarbon fuels. Hydrogen's wide flammability limits, high reactivity—linked to its fast and simple chemical kinetics—and its high molecular diffusivity lead to fundamentally different flame behaviours [1]. These include a strong tendency to flashback, enhanced propensity for thermoacoustic instabilities, higher adiabatic flame temperatures, and higher laminar flame speeds. Such characteristics complicate the design of stable and efficient combustors, particularly when targeting ultra-low NO_x emissions [2]. Flame flashback, in particular, represents a major safety concern, as it can cause upstream flame propagation and potentially damage the fuel injection system [2]. Additionally, the high flame temperatures intrinsic to hydrogen combustion promote thermal NO_x formation via the Zeldovich mechanism, especially in non-premixed regimes.
Various combustor designs have been proposed to enable pure hydrogen combustion while maintaining operational stability and emissions compliance [3–5]. Among these, dual-swirl configurations with coaxial jets have shown promise. These designs utilize aerodynamic swirl to enhance mixing and stabilize the flame. Typically, the configuration consists of a central swirling jet surrounded by an annular swirling air stream. In these setups, the central jet is either composed of pure hydrogen [5] or a premixed mixture of pure hydrogen and air [4], while the annular jet carries only air.
Multi-coaxial swirlers are frequently implemented in gas turbine combustors to improve the mixing of air and fuel, thereby enhancing combustion efficiency [6]. Compared to single-swirler setups, coaxial swirl systems exhibit more intricate flow behavior due to the interaction between the swirling jets, which generates complex flow structures that can influence flame stability and emissions. Several studies have explored how variations in swirl intensity and rotational direction—such as co-rotating and counter-rotating configurations—impact the flow field and combustion

DOI: 10.13009/EUCASS2025-404

characteristics, offering valuable insights into their role in pollutant formation and overall combustion performance [7–11].

Dual-swirl injectors, characterized by both inner and outer swirling flows, offer several potential advantages for hydrogen combustion. The introduction of an additional control parameter—the inner jet swirl level—combined with the outer swirl level, enables control over flame stabilization and structure, and helps reduce NO_x emissions through overall lean combustion strategies [4,10].

The literature highlights the complex interplay between flame shape, swirl number, momentum flux ratio, and hydrogen injection parameters on both stability and NO_x emissions [4,10,12,13]. Different flame stabilization regimes−including attached M-shaped flames and lifted V-shaped flames−were observed depending on operating parameters such as thermal power, secondary air flow rate, and swirl intensity in both jets. These regimes have significant implications for combustion efficiency and pollutant formation [10,12,14].

Leroy et al. [15] investigated the effect of air staging between two non-swirling coaxial jets on flame length, flame topology, and NO_x emissions. Two configurations were analyzed: a central non-premixed (diffusive) injection and a central rich premixed H_2/air mixture injection, with central equivalence ratios in the range $2 \leq \Phi_p \leq 6$. The introduction of a rich premixed fuel–air mixture was found to reduce the total flame length compared to the non-premixed configuration, mainly due to a shift in the stoichiometric mixture fraction between the two streams. Moreover, as the central equivalence ratio approaches $\Phi_p = 2$, a premixed flame front is stabilized, further reducing the flame length. Air staging in the coaxial injector also led to lower NO_x emission indices, primarily due to a reduction in the height of the diffusion flame, which is mainly responsible for NO_x formation.

In a separate study, Leroy et al. [16] analyzed NO_x emissions in a dual-swirl injector fueled with 100% H_2. The study examined stoichiometric and rich premixed central jets with equivalence ratios up to $\Phi_p = 6$. They identified different flame structures depending on the inner and outer swirl levels, the momentum flux ratio (J), and the central equivalence ratio. NO_x emissions varied significantly across these configurations; notably, the lowest $EINO_x$ level was observed in the case with the richest central jet ($\Phi_p = 4$) and a high momentum flux ratio $J = 54.9$.

For the dual-swirl non-premixed configuration, a recent publication reports that at 18 kW thermal power and a global equivalence ratio of $\Phi_g = 0.6$, strong high-frequency self-sustained pressure oscillations occur [17]. These oscillations are attributed to a synchronization with hydrodynamic helical vortical disturbances and a rotating acoustic wave coupled to the first degenerate transverse mode of the symmetric combustion chamber [17].

A dual-swirl injector, referred to as the Rich-premixed, Air-staged, Dual-Swirl Injector for Hydrogen (RAPIDS-H), has been designed and experimentally investigated at the Combustion and Optical Diagnostics Laboratory of Politecnico di Milano. The system implements a radially staged injection strategy, consisting of a centrally positioned rich-premixed swirl jet surrounded by a co-rotating annular air stream. Premixing in the central jet is achieved by combining hydrogen and air just upstream of the injector exit. Hydrogen is injected axially while air is injected tangentially at a 90° angle, promoting rapid mixing and swirl generation. This fast mixing, occurring close to the injector exit, may help mitigate the risk of flashback—a critical concern with hydrogen due to its high diffusivity and flammability. A previous rich-premixed dual-swirl configuration was initially developed and preliminary tested with natural gas and GN/H_2 [18,19], while the isothermal flow structure for different swirl levels of the central and outer jets was investigated by Cozzi et al.[11]. Compared to these earlier studies, the current injector geometry has been slightly changed by altering the size and distribution of the injection holes to achieve a more uniform distribution of air and H_2 flows and by enlarging the diameter of the inner jet. An experimental analysis of the isothermal flow field structure generated by two different versions of the RAPIDS-H injectors (models A and B), at the exactly the same flow rate conditions, has been conducted by Stereo-PIV by Iapaolo et al. [20]. The experimental results evidence that the injector with a higher geometrical swirl number, i.e., injector A, produced a more intense central recirculation zone (CRZ) than injector B. Moreover, vortex breakdown occurred closer to the burner outlet for Injector A, influencing the extent and position of the recirculation regions.

To our knowledge, the dual-swirl configuration operating with highly rich premixed mixtures of pure hydrogen and air, with central jet equivalence ratios $\Phi_p > 2$, has not been fully investigated; thus, the present paper aims to present some experimental results on flame stability, morphology and pollutant emissions obtained on RAPIDS-H injector (model A) when operating with a rich-premixed H_2/air central jet.

2. The combustion chamber and the RAPIDS-H injector

The RAPIDS-H system features two coaxial cylindrical ducts with a central rich-premixed swirl injector surrounded by an annular swirling air stream, housed in an octagonal combustion chamber (apothem 96.5 mm). The chamber has four stainless steel walls and four quartz windows for optical access, and a top-mounted hood that allows insertion of a gas sampling probe for exhaust gas analysis, as shown in Figure 1.

DOI: 10.13009/EUCASS2025-404

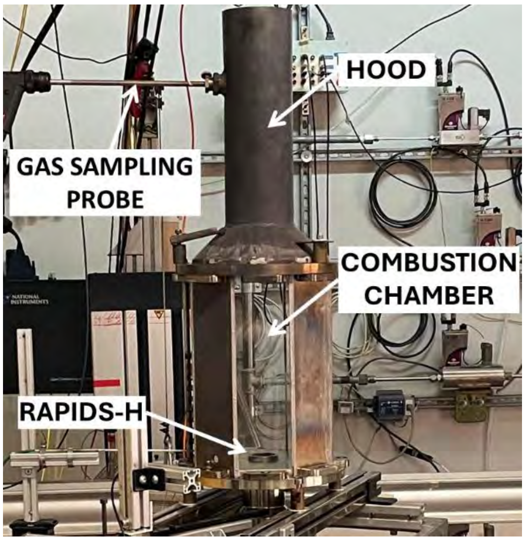

Figure 1: Combustion chamber.

The swirling motion of the coaxial air flowing in the annular section of the injector is generated upstream inside a cylindrical plenum by an axial plus tangential air injection and its intensity is controlled via the respective mass flow rates $\dot{m}_{s,tan}$ and $\dot{m}_{s,ax}$. The geometric swirl number of the annular air jet, $S_{g,s}$, is given by Eq. (1):

$$S_{g,s} = \frac{\pi R_{0,s} D}{2A_{T,s}} \left(\frac{\dot{m}_{s,tan}}{\dot{m}_{s,tan} + \dot{m}_{s,ax}} \right)^2 \tag{1}$$

where $R_{0,s} = 38\ mm$ is the radial distance from tangential port to axis, $D = 36\ mm$ is the swirler outlet diameter and $A_{T,s}$ is the total cross-sectional area of tangential air channels.

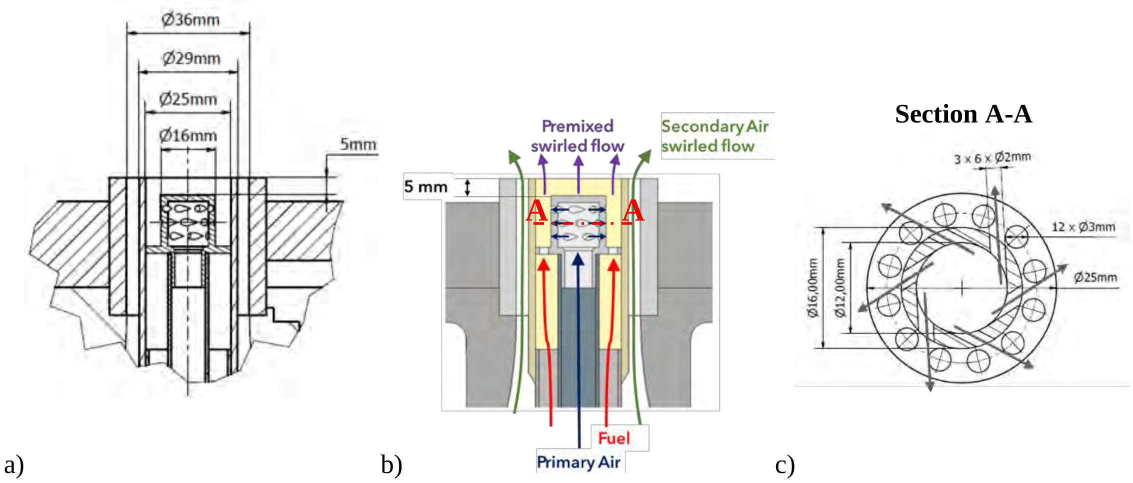

Figure 2: a) Detail of the RAPIDS-H injector. b) Distribution of fluid flows in the injector .c) Cross-sectional view of the central injector head; the arrows indicate the direction of the premixing air injection.

The central injector (Figure 2) has a body diameter $D_{inj} = 16\ mm$ and is recessed by $5\ mm$ into a duct of internal diameter $D_{p,i} = 25\ mm$. Tangential air is injected through 3 rows of 6 holes each with diameter $D_{tan} = 2\ mm$, while hydrogen is injected axially through 12 crown holes of diameter $D_{ax} = 3\ mm$. The crown's external diameter matches the $25\ mm$ duct, leaving minimal gap. The air and hydrogen injection ports are arranged orthogonally to maximize mixing. The geometric swirl number of the premixed stream, $S_{g,p}$, and the premixed equivalence ratio Φ_p, are not independent, but are related through Eq. (2), which is illustrated in Figure 3:

$$S_{g,p} = \frac{M_{mix}}{M_{air}} \frac{2R_{o,p} D_{p,i}}{18 D_{tan}^2} \left(\frac{1}{1 + \Phi_p f_{stech}} \right)^2 \tag{2}$$

DOI: 10.13009/EUCASS2025-404

where $R_{0,p} = 5$ mm is the distance of the tangential ports from the injector axis, $f_{\text{stech}} \cong 0.0292$ is the stoichiometric fuel-air ratio on a mass basis, M_{mix} and M_{air} are the molar mass of the H_2/air mixture and air. The molar mass ratio accounts for the density difference between axial and tangential flows. As clearly shown in Figure 3 enriching the premixed jet – i.e. increasing Φ_p – leads to a decrease in the swirl number.

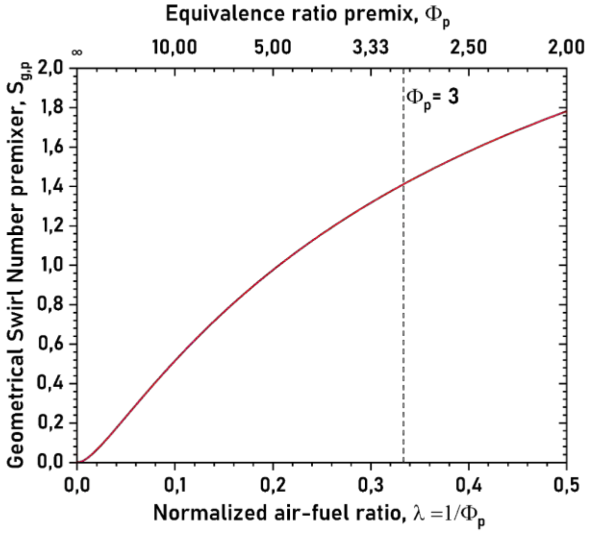

Figure 3: Geometrical swirl number of the premixed jet, $S_{g,p}$, vs. the premixed equivalence ratio Φ_p

The premixing and global equivalence ratios, Φ_p and Φ_g respectively, are calculate using Eqs. (3):

$$\Phi_p = \frac{\dot{m}_{H_2}}{\dot{m}_{air,p} f_{stech}}; \qquad \Phi_g = \frac{\dot{m}_{H_2}}{(\dot{m}_{s,tan} + \dot{m}_{s,ax} + \dot{m}_{air,p}) f_{stech}} \tag{3}$$

where $\dot{m}_{air,p}$ is the premixing air mass flow rate and $\dot{m}_{H_2}$ represents the hydrogen mass flow rate. Finally, the momentum flux ratio J between the annular and central jets is computed as per Eq. (4):

$$J = \frac{momentum\, flux\, outer\, jet}{momentum\, flux\, inner\, jet} = \left(\frac{A_p}{A_s}\right)^2 \frac{(\Phi_p/\Phi_g - 1)^2}{(1 + \Phi_g f_{stech})(1 + M_{air} \Phi_g f_{stech}/M_{H2})} \tag{4}$$

with M_{H2} representing the molar mass of hydrogen. The cross-sectional area of the central injector is $A_p = \pi D_{p,i}^2/4$, while that of the annular section is $A_s = \pi\left(D^2 - D_{p,s}^2\right)/4$, where $D_{p,s} = 29\ mm$ is the outer diameter of the central injector. As shown in Eq. (4), the momentum flux ratio depends on the global and premixing equivalence ratios and on injector geometry through the area ratio A_p/A_s.

3. Experimental setup and operating conditions

The experimental setup consists of the burner, the air and fuel supply system, the optical apparatus and the exhaust gas analyzer. Hydrogen of 99.999% purity, supplied from cylinders, was used as fuel. Hydrogen and air flow rates are set and measured through thermal mass flowmeters with maximum uncertainty of 1.4%. Burner monitoring and data acquisition are performed through a homemade control program.

Two different CMOS cameras were used for UV imaging. The first camera is a global shutter monochromatic camera based on the IMX487 CMOS sensor. It has a resolution of 2840×2840 pixels with a pixel pitch of $2.74\ \mu m$. The sensor is specifically designed for UV imaging, and the manufacturer reports a quantum efficiency of approximately 48% at $310\ nm$. The camera is fitted with a $50\ mm$ $F/2.8$ ultraviolet lens (200– $1000\ nm$) and the same Near-UV Bandpass Filter used with the first camera. Images are acquired with an aperture of $F/5.6$, an exposure time of $600\ ms$, and no gain applied. The camera is positioned approximately $0.9\ m$ from the burner axis, and the image has been cropped to a field of view of approximately 7×9 cm. The second is a monochromatic camera with a rolling shutter operating in global reset mode. According to the manufacturer, it has a quantum efficiency greater than 20% at $310\ nm$. The camera features a resolution of 3072×2048 pixels with a pixel pitch of $2.40\ \mu m$. It is equipped with a $75\ mm$ $F/3.8$ ultraviolet lens (spectral range: 200– $1000\ nm$), and a Near-UV Bandpass Filter. The transmissivity of

DOI: 10.13009/EUCASS2025-404

the bandpass filter exceeds 50% between $300\text{–}360\,nm$, with a peak value of 72% at $310\,nm$. The camera is positioned approximately $1.15\,m$ from the burner axis, and the image has been cropped to a field of view of approximately 7×9 cm. Images are acquired with an aperture of $F/8$, an exposure time of $300\,ms$, and a gain setting of $17\,dB$.
For each operating condition, a set of 40 to 100 UV images was acquired while the burner operated in steady-state mode. The images were averaged, and only the resulting mean images are presented in this work.
A checkerboard target is placed along the burner axis inside the combustion chamber to acquire calibration images. Knowing the physical dimensions of the target, a scale factor can be calculated to calibrate the images. When converting pixel coordinates to physical units, the origin of the vertical axis is set at the exit plane of the RAPIDS-H injector, and the coordinates are normalized by the injector diameter, $D = 36\,mm$.
A gas analyzer is used to measure the exhaust gas composition, and a type-K thermocouple placed at the tip of the sampling probe allows for measuring the gas temperature, T_{gas}, with an uncertainty of 2%. The gas analyzer is equipped with electrochemical sensors to measure: O_2 percentage with an uncertainty of 0.2%, NO and NO_2 with an uncertainty of $2\,ppm$ and H_2 with uncertainty equal to $10\,ppm$. The sampling probe is inserted horizontally in the hood in correspondence with the burner axis, at a height from the injector outlet of $55\,cm$ (see Figure 1), and exhaust hot gases are collected at stationary operating conditions and the measured concentrations are averaged over a period of 1 minute. All emissions are on a dry base.
To normalize the NO_x emissions level the emission index $EINO_x$ in g/kg_{H2} is computed through Eq. (5) using the measured molar fraction $X_{NO_x,dry}$ (in ppm):

$$EINO_x = \frac{X_{NOx,dry}}{1000}\frac{1}{2}\left(\frac{4.76}{\Phi_g} - 1\right)\frac{M_{NO2}}{M_{H2}} \quad (5)$$

in which M_{NO2} is the molar mass of NO_2, as most NO is converted to NO_2 in the atmosphere, Eq. (5) is obtained assuming only H_2O, O_2, and N_2 in the combustion products.
Combustion efficiency, η_c, is defined as the ratio between the fuel converted to H_2O and the original fuel amount. The former is estimated based on the molar fraction of H_2 measured in the exhaust, X_{H2}, as per Eq. (6):

$$\eta_c = 1 - \frac{X_{H2}}{(2-3X_{H2})}\left(\frac{4.76}{\Phi_g} - 1\right) \quad (6)$$

Eq. (6) is obtained assuming complete combustion and only H_2O, H_2, O_2, and N_2 in the combustion products. Under all tested conditions, the concentration of H_2 in the exhaust was extremely low, and the combustion efficiency remained consistently above 99.7%. The investigated operating conditions are summarized in Table 1.

Table 1: Nominal thermal power, global and premixed equivalence ratio and geometrical swirl numbers

Parameter	**Operating Values**
Nominal thermal Power, kW	12
Global equivalence ratio, Φ_g	0.25 – 0.35 – 0.45
Premixed equivalence ratio, Φ_p	3 – 5 – 7 – 9
Geometrical swirl number – premix, $S_{g,p}$	1.41 – 0.98 – 0.73 – 0.57
Geometrical swirl number – secondary air, $S_{g,s}$	from 4.4 to 22.2

4. Experimental Results

4.1 Combustion Stability

From the perspective of static stability, the injector exhibits flashback phenomena when operating at premixed equivalence ratios Φ_p equal to or less than 5, with the severity of flashback varying as a function of Φ_p.
Flashback initially manifests at $\Phi_p = 5$ with the appearance of small flames, visible to the naked eye, inside the central injector. Due to the injector geometry, which limits clear visual access, it is not possible to precisely determine the

DOI: 10.13009/EUCASS2025-404

location of these flames. However, it is reasonable to assume they occur in correspondence with the air jets, where the local equivalence ratio is close to unity, although it remains unclear whether all air jets or only some are involved. Under this condition, continuous operation for more than 15 minutes does not lead to visible injector overheating; therefore, this regime has been identified as mild flashback, and measurements performed under these conditions have been included in the analysis.

Reducing Φ_p to a sufficiently low value ($\Phi_p = 3$ for $\Phi_g = 0.45$, and $\Phi_p < 3$ for lower Φ_g) causes the outer conduit of the central injector (25 mm internal diameter, shown in Figure 2a) to glow red almost immediately. This necessitates test termination to prevent thermal damage to the hardware. This condition is referred to as strong flashback, and no measurements are taken under these circumstances.

It remains unclear whether the observed flashback is of the boundary-layer type—initiated by the flame anchored at the injector lip propagating upstream along the inner wall of the outer conduit—or caused by autoignition of the fuel/air mixture due to hot recirculating gases.

The distinction between mild and strong flashbacks can be attributed to changes in local stoichiometry and reductions in the annular cold air flow as Φ_p decreases, which result in different flashback intensities and effects. Specifically, at constant Φ_g and thermal power, reducing Φ_p increases the amount of air available for combustion inside the injector, thereby increasing heat release. Simultaneously, the annular air flow rate decreases, reducing its effectiveness in cooling the outer wall of the central injector.

Moreover, boundary-layer flashback is known to be influenced by thermal coupling between the flame front and the burner structure [21]. This coupling may lead to localized wall heating, further promoting flame propagation upstream and ultimately triggering injector flashback under sufficiently adverse conditions.

A key operational feature is that strong flashback can be reversed without extinguishing the burner. Simply removing the premixed air supply causes the small flames inside the injector to self-extinguish, and a fully diffusive flame re-establishes itself outside the central nozzle, resembling that observed under standard operating conditions. Notably, during this transition, no blow-off was ever observed, confirming the effectiveness and stability of the procedure.

Although blow-off was not thoroughly investigated, it was not observed under any of the tested conditions. The flame remained steadily anchored to the burner down to the lowest global equivalence ratio tested, which was 0.25.

4.2 Flame morphology

In all the conditions analyzed, the flame front consistently maintains an M-shaped structure due to the establishment of reverse flow in the central region of the combustion chamber, as highlighted by the flame image captured with a color still camera without any optical filter and shown in Figure 4, with the central V-shaped valley flattening as the premixing equivalence ratio increases. Additionally, for experimental conditions corresponding to a flammable premixed mixture ($\Phi_p \lesssim 7.57$ [22]), a rich-premixed conical flame never appears in the images, Figure 5 - Figure 7. As noted by Leroy et al. [16], this absence may be attributed either to the UV camera failing to detect it or, for $\Phi_p > 5$, to the flame being blown off.

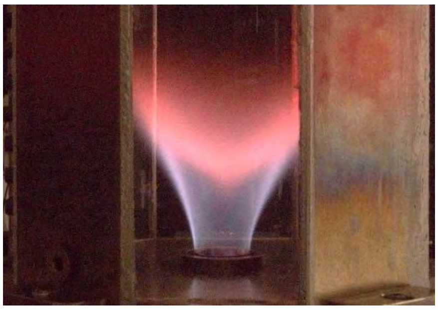

Figure 4: Visible flame image at $S_{g,s} = 9.8$, $P_{th} = 12\ kW$, $\Phi_p = 5$, $\Phi_g = 0.45$, $2\ s$ exposure time

Generally, the flame remains anchored to the central injector lip and exhibits a diffusive reaction layer with a light grayish-blue color, associated with broadband visible emissions and located in the shear layer between the annular air jet and the central premixed jet. The upper part of the flame is predominantly red but exhibits a subtle shift toward violet and magenta hues depending on the operating parameters, without ever becoming blue. The red coloration is most likely generated by the spontaneous emission of vibrationally excited H_2O molecules [23], whereas the observed shift toward violet and magenta may arise from an overlapping broadband light blue emission.

The flame morphology, revealed by average chemiluminescence images taken with the IMX487 CMOS camera highlighting regions associated with the presence of OH^* radicals [23], is shown in Figure 5 - Figure 7 for a geometric swirl number of $S_{g,s} = 9.8$, global equivalence ratios $\Phi_g = 0.25$, 0.35 and 0.45 and varying premixed equivalence

DOI: 10.13009/EUCASS2025-404

ratios, Φ_p. For all three Φ_g values, the flame morphology exhibits a consistent pattern as Φ_p is varied. (see Figure 5 - Figure 7). Under the condition $\Phi_g = 0.45$ and $\Phi_p = 3$, a strong flashback event was observed, causing the outer wall of the premixed injector to rapidly glow red. To prevent thermal damage to the hardware, this operating condition was excluded from further investigation, and no chemiluminescence images were recorded for this condition.
Within the investigated parameter range, the images clearly show a modest yet non-negligible dependence of flame geometry on both equivalence ratios. Specifically, for a fixed global equivalence ratio (Φ_g), the flame height slightly decreases as the premixed equivalence ratio (Φ_p) increases from 3 (under mild flashback conditions) to 5 (still under mild flashback conditions), while the flame front region near the injector becomes brighter and sharper (Figure 5d vs Figure 5c). Furthermore, as the premixed equivalence ratio increases, the flame base appears to move closer to the injector.

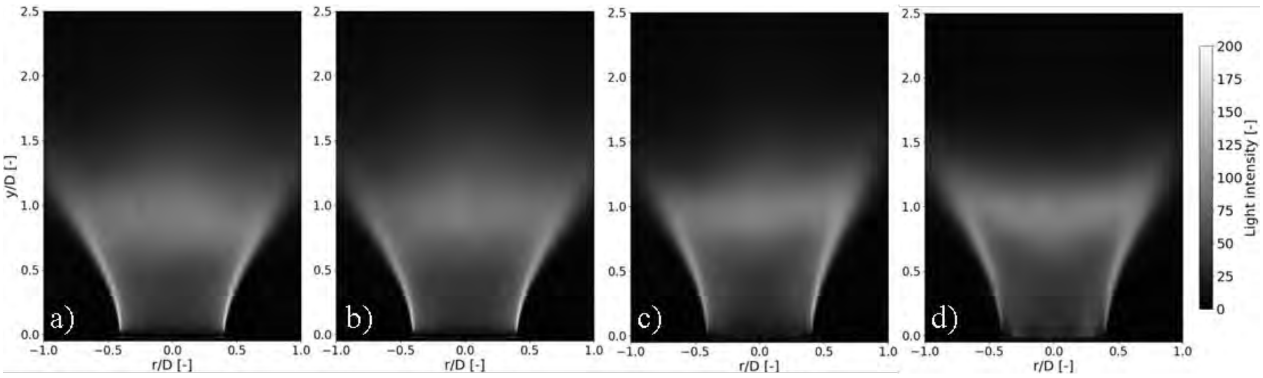

Figure 5: Mean OH^* images at $S_{g,s} = 9.8$, $\Phi_g = 0.25$. a) $\Phi_p = 9$ b) $\Phi_p = 7$ c) $\Phi_p = 5$ d) $\Phi_p = 3$.

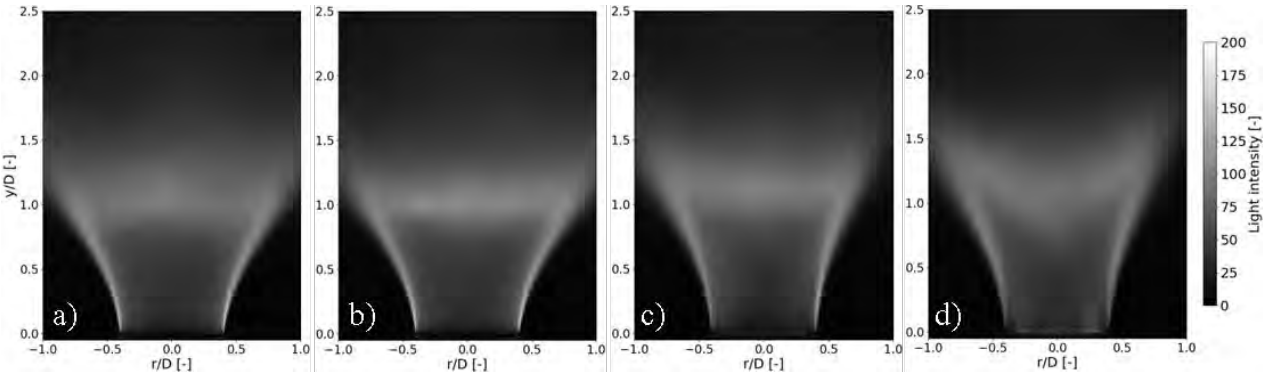

Figure 6: Mean OH^* images at $S_{g,s} = 9.8$, $\Phi_g = 0.35$. a) $\Phi_p = 9$ b) $\Phi_p = 7$ c) $\Phi_p = 5$ d) $\Phi_p = 3$.

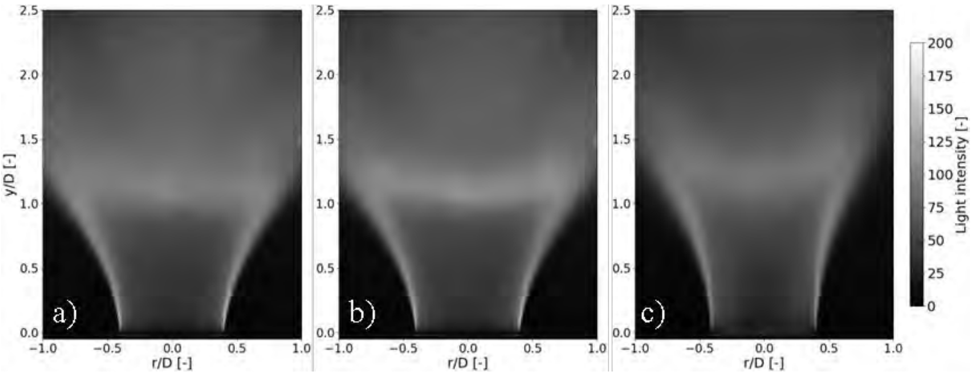

Figure 7: Mean OH^* images at $S_{g,s} = 9.8$, $\Phi_g = 0.45$. a) $\Phi_p = 9$ b) $\Phi_p = 7$ c) $\Phi_p = 5$.

At $\Phi_p = 3$, weak luminous tongues are visible in the OH^* chemiluminescence images near the injector outlet (Figure 5d and Figure 6d), indicating localized flashback-induced flames. At $\Phi_p = 5$, these features are barely visible. Increasing Φ_p to 7 leads to a further slight decrease in flame height and enhanced compactness and brightness of the flame front near the injector, with no evidence of flashback and no visible luminous tongues. A further increase to $\Phi_p = 9$ does not produce significant changes in flame morphology. Overall, a reduction in flame height is associated with a faster radial expansion of the flame front along the axial direction.

DOI: 10.13009/EUCASS2025-404

At constant thermal power and global equivalence ratio (Φ_g), increasing the premixed equivalence ratio (Φ_p) leads to a higher air flow rate in the annular jet and a reduced momentum and swirl intensity in the central jet. As a result, it is hypothesized that the central jet interacts less effectively with the recirculation zone, allowing hot combustion products to approach the injector more closely. The flow redistribution also increases both the velocity difference between the two jets and the momentum flux ratio J (Figure 8a-b), thereby enhancing turbulent mixing between the annular air and the rich premixed jet. Overall, it is hypothesized that the reduction in central jet flow rate and the resulting improvement in mixing efficiency outweigh the opposing influence of the higher local equivalence ratio, which would otherwise tend to lengthen the flame, leading to a net decrease in flame height.
For constant values of Φ_p, a progressive reduction in flame length is observed as Φ_g decreases (see Figure 5 Figure 7). This reduction in Φ_g is achieved by increasing the air flow rate in the annular co-axial jet, while keeping the air and hydrogen flow rates in the central injector fixed. As a result, lower Φ_g values correspond to a greater velocity difference between the two jets (Figure 8b), which enhances turbulent mixing between the annular air and the central premixed jet. This more efficient mixing intensifies combustion near the injector and ultimately leads to a shorter flame

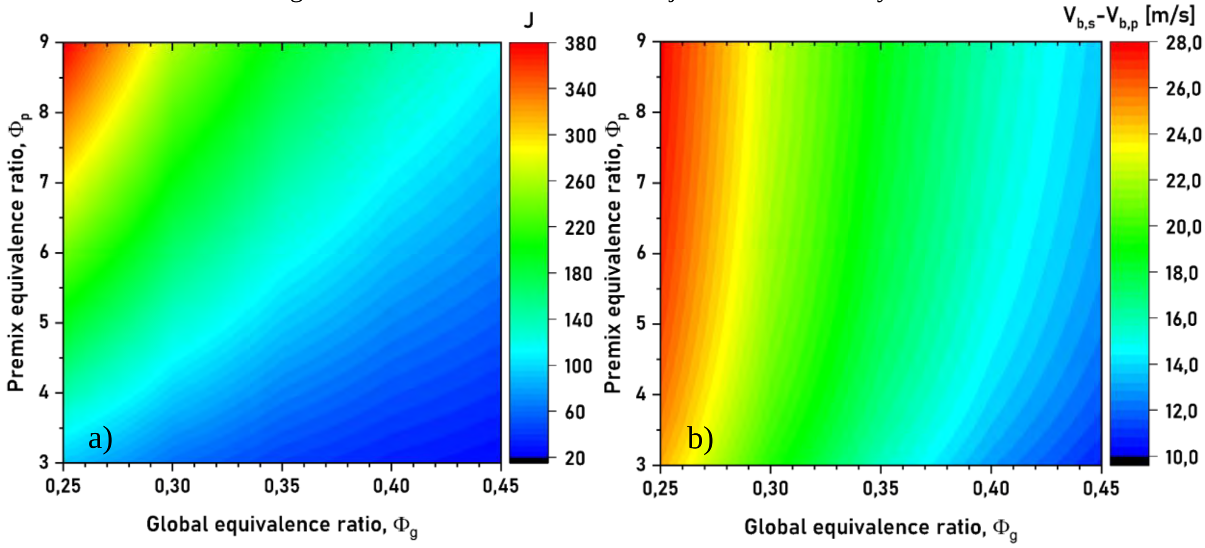

Figure 8: (a) Momentum flux ratio J. (b) Difference between bulk velocity of the annular air jet, $V_{b,s}$, and bulk velocity of the premixed jet, $V_{b,p}$.

The effect of the secondary swirl number $S_{g,s}$ on flame morphology was analyzed in a previous work [24] and is briefly summarized here for completeness. The investigated case corresponds to a thermal power of $P_{th} = 12\ kW$, $\Phi_p = 5$ and $\Phi_g = 0.45$, while the examined swirl numbers were $S_{g,s} = 4.4$, 6.8, 13.4, and 22.2. Chemiluminescence images for these conditions, shown in Figure 9, were acquired using the rolling shutter camera.

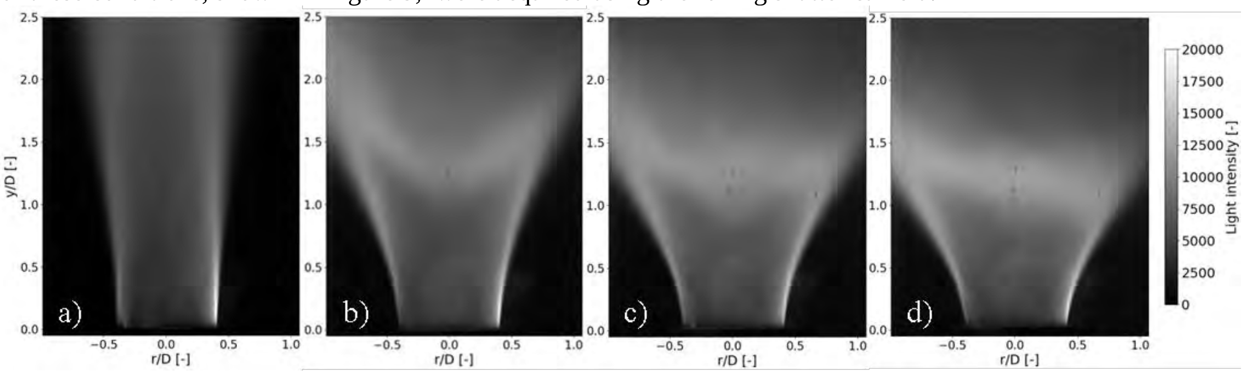

Figure 9: Mean OH^* images ($\Phi_p = 5$, $\Phi_g = 0.45$). a) $S_{g,s} = 4.4$ b) $S_{g,s} = 6.8$ c) $S_{g,s} = 13.4$ d) $S_{g,s} = 22.2$.

Results showed that at the lowest swirl level, $S_{g,s} = 4.4$, the flame morphology resembles a jet flame (Figure 9a). While the flame base appears stable and attached to the injector, the downstream region exhibits a counter-clockwise precessing motion. This motion is likely caused by a combination of the imposed swirl and the conical contraction of the hood, which may induce a downstream vortex breakdown along with a precessing vortex core (PVC) instability.
Increasing the swirl level to $S_{g,s} = 6.8$ leads to a shorter flame that transitions from a jet-like shape to an M-shaped structure, as a reverse flow establishes in the central region of the combustion chamber. Further increases in $S_{g,s}$ result in flames that retain the M-shape, with the central V-shaped valley flattening as swirl level increases, but become even

DOI: 10.13009/EUCASS2025-404

shorter and slightly wider, with more rapid radial spreading with increasing axial distance compared to lower swirl levels (Figure 9b,c,d).
Overall, the geometrical swirl number $S_{g,s}$ has a significant impact on flame morphology, particularly between 4.4 and 6.8. Beyond this range, further increases primarily affect the flame size, while the M-shape remains almost unchanged.

4.3 NOx emissions

NO_x measurements were repeated for selected test conditions and showed good repeatability. However, under the very lean conditions investigated here, the relative accuracy of the measurements decreases due to the high excess air in the combustion gases, which dilutes the emissions (see Eq. (5)). As a result, these measurements should be interpreted with caution.
At $S_{g,s} = 9.8$ and under all tested conditions, $EINO_x$ emissions, expressed as grams of NO_x produced per kilogram of hydrogen, remain within the range of $1.72\ g/kg_{H2}$ to $2.75\ g/kg_{H2}$, as shown in Figure 10a. This range partially overlaps with the data reported by Leroy et al. [16], who measured $EINO_x$ values between $0.66\ g/kg_{H2}$ and $4.47\ g/kg_{H2}$ for a dual-swirl injector operating at $10\ kW$, with global and premixed equivalence ratios (Φ_g and Φ_p) similar to those used in the present study. It is worth noting that the injector used by Leroy et al. is smaller than the one employed here, resulting in higher flow velocities in both the central and annular swirled jets. These differences, along with possible variations in flame morphology, may help explain both the broader range and the discrepancies observed between our dataset and theirs.

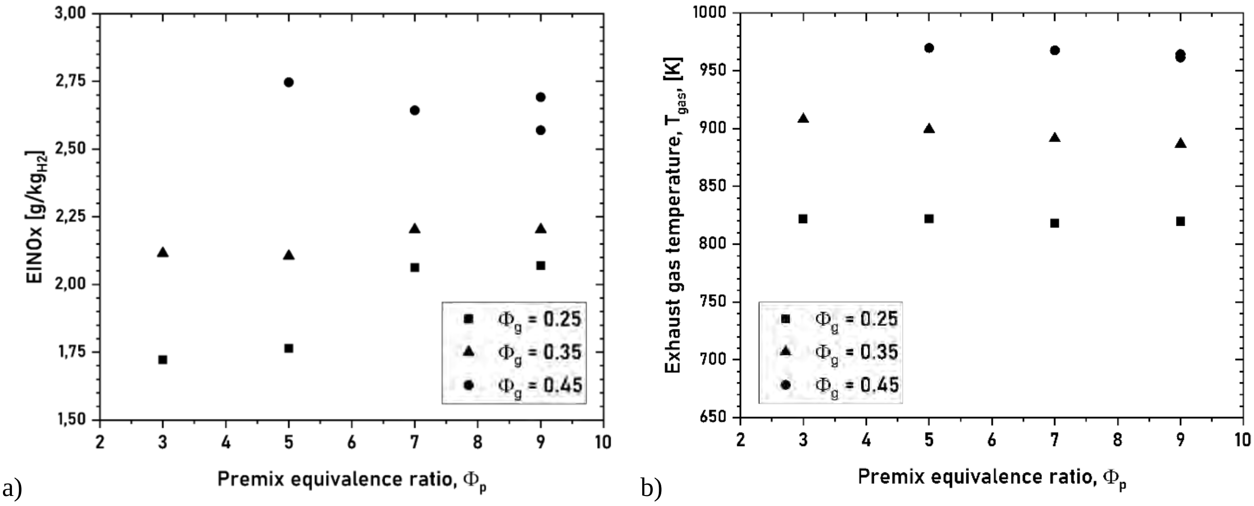

Figure 10: (a) $EINOx$ emissions (grams of NOx per kilogram of H_2, g/kg_{H2}). (b) Exhaust gas temperature.

As shown in Figure 10a, both Φ_g and Φ_p influence the measured NO_x emissions. The highest $EINO_x$ value, approximately $2.75\ g/kg_{H2}$, is observed at $\Phi_g = 0.45$ and $\Phi_p = 5$. At this fixed Φ_g, increasing Φ_p results in a slight decrease in $EINO_x$. A decrease in the global equivalence ratio leads to a progressive reduction in $EINO_x$, with values dropping below approximately $2.2\ g/kg_{H2}$ and reaching a minimum of about $1.72\ g/kg_{H2}$ at $\Phi_g = 0.25$ and $\Phi_p = 3$. This trend is likely attributable to a combination of lower gas temperatures, T_{gas}, (Figure 10b) and reduced flame size, as discussed in the previous section. The conditions at $\Phi_p = 5$ and $\Phi_p = 3$ appear to be the most sensitive to changes in Φ_g. Specifically, at $\Phi_p = 5$, $EINO_x$ decreases from $2.75\ g/kg_{H2}$ to $1.76\ g/kg_{H2}$ as Φ_g is reduced from 0.45 to 0.25 (Figure 10a).
For $\Phi_g = 0.35$ and $\Phi_g = 0.45$, $EINO_x$ is almost insensitive to changes in Φ_p. In contrast, at $\Phi_g = 0.25$, a strong reduction in $EINO_x$ is observed when decreasing Φ_p (Figure 10a). As noted earlier, the limited measurement accuracy under very lean conditions requires these results be interpreted with caution. If the behavior at $\Phi_g = 0.25$ is confirmed, it may indicate that the occurrence of mild flashback ($\Phi_p \leq 5$), characterized by small diffusion flames within the injector, plays a role in NO_x formation. Nevertheless, either due to the limited size of these diffusion flames, or because the NO_x they produce is offset by reduced formation in the main M-shaped flame, the overall effect under mild flashback conditions is a lower $EINO_x$ level.

DOI: 10.13009/EUCASS2025-404

5. Conclusions

The experimental investigation conducted on a rich-premixed, hydrogen-fueled dual-swirl burner (RAPIDS-H) yielded significant insights into its combustion characteristics and NO_x emissions. The burner's design—featuring a centrally located, rich-premixed swirling hydrogen–air jet surrounded by an annular swirling air stream—demonstrated effective flame stabilization across a wide range of operating conditions. An M-shaped flame structure, with the central V-shaped region flattening as the premix equivalence ratio (Φ_p) increases, was consistently observed.

A key finding was that decreasing the global equivalence ratio (Φ_g)—i.e., increasing the air flow rate in the outer jet—resulted in a shorter flame, possibly due to enhanced mixing driven by the increased inner-to-outer jet velocity difference and momentum flux ratio. At $\Phi_p = 5$, small flames appeared inside the mixing region of the central injector. This flashback condition, classified as mild flashback, did not cause visible overheating of the injector hardware and allowed stable operation. However, at $\Phi_p = 3$ and $\Phi_g = 0.45$, the central injector immediately began to glow red-hot. This severe flashback condition was unsustainable but could be quickly mitigated without flame extinction by simply cutting off the premixed air flow. A key operational feature is that such strong flashback can be reversed without shutting down the burner: removing the premixed air supply causes the small flames inside the injector to self-extinguish, allowing a fully diffusive flame to re-establish itself outside the central nozzle. Notably, no blow-off was ever observed during this transition, confirming both the effectiveness and stability of the procedure. Furthermore, blowoff was not encountered within the tested range of conditions.

NO_x emissions (expressed as $EINOx$) show encouragingly low levels, ranging approximately 1.7 to 2.8 g/kg_{H2}. They also exhibit a strong sensitivity to the global equivalence ratio (Φ_g) with consistently reduced $EINO_x$ observed at lower values of Φ_g. This trend may be primarily attributed to decreased flame temperature and smaller flame size, which are known to limit thermal NO_x formation. In contrast, noticeable sensitivity to premixed equivalence ratio (Φ_p) was observed only at $\Phi_g = 0.25$. Nonetheless, the limited measurement accuracy of NO_x concentrations under very lean conditions requires that these results be interpreted with caution.

Under all tested conditions, the concentration of H_2 in the exhaust was extremely low, and the combustion efficiency consistently exceeded 99.7%, indicating near-complete fuel oxidation.

These findings highlight the complex interplay between burner operating parameters and NO_x formation in rich-premixed hydrogen combustion. The results emphasize the potential of this dual-swirl configuration to enable stable, low-NO_x operation. Future work should include a more detailed analysis of the flashback phenomenon in order to develop design strategies that increase the burner's resistance to flashback. In addition, further investigation of the flame and flow-field structure and their influence on NO_x formation pathways—through advanced diagnostics and numerical modelling— could enhance the fundamental understanding and support the further optimization of burner designs for hydrogen combustion applications.

Acknowledgements

The development of this work is framed in the Environmentally Friendly Aviation for All Classes of Aircraft (EFACA) project. This project is funded by the European Union Horizon Europe research and innovation programme (HORIZON-CL5-2021-D5-01-05) under grant agreement no.101056866.

References

[1] Pitsch, H. 2024. The transition to sustainable combustion: Hydrogen- and carbon-based future fuels and methods for dealing with their challenges. *Proc. Combust. Inst.* 40:105638.

[2] Giacomazzi, E., G. Troiani, A. Di Nardo, G. Calchetti, D. Cecere, G. Messina, and S. Carpenella. 2023. Hydrogen combustion: Features and barriers to its exploitation in the energy transition. *Energies* 16:7174.

[3] Cecere, D., E. Giacomazzi, and A. Ingenito. 2014. A review on hydrogen industrial aerospace applications. *Int. J. Hydrogen Energy* 39:10731–1047.

[4] Leroy, M., C. Mirat, A. Renaud, and R. Vicquelin. 2023. Stabilization of low-NOx hydrogen flames on a dual-swirl coaxial injector. *J. Eng. Gas Turbines Power* 145.

[5] Marragou, S., H. Magnes, A. Aniello, L. Selle, T. Poinsot, and T. Schuller. 2022. Experimental analysis and theoretical lift-off criterion for H_2/air flames stabilized on a dual swirl injector (submitted). *Proc. Combust. Inst.*

[6] Liu, Y., X. Sun, V. Sethi, D. Nalianda, Y. G. Li, and L. Wang. 2017. Review of modern low emissions combustion technologies for aero gas turbine engines. *Prog. Aerosp. Sci.* 94:12–45.

[7] Merkle, K., H. Haessler, H. Büchner, and N. Zarzalis. 2003. Effect of co- and counter-swirl on the isothermal flow- and mixture-field of an airblast atomizer nozzle. *Int. J. Heat Fluid Flow* 24:529–37.

DOI: 10.13009/EUCASS2025-404

[8] Yuasa, S. 1986. Effects of swirl on the stability of jet diffusion flames. *Combust. Flame* 66:181–92.
[9] Sung, Y., and G. Choi. 2016. Non-intrusive optical diagnostics of co- and counter-swirling flames in a dual swirl pulverized coal combustion burner. *Fuel* 174:76–88.
[10] Marragou, S., H. Magnes, T. Poinsot, L. Selle, and T. Schuller. 2022. Stabilization regimes and pollutant emissions from a dual fuel CH_4/H_2 and dual swirl low NOx burner. *Int. J. Hydrogen Energy* 47:19275–88.
[11] Cozzi, F., A. Francabandiera, and L. Zampini. 2023. Flow field investigation of confined coaxial swirling jets by Stereo-PIV. *J. Phys. Conf. Ser.* 2590:012011.
[12] Aniello, A., D. Laera, S. Marragou, H. Magnes, L. Selle, T. Schuller, and T. Poinsot. 2023. Experimental and numerical investigation of two flame stabilization regimes observed in a dual swirl H_2-air coaxial injector. *Combust. Flame* 249:112595.
[13] Vilespy, M., A. Aniello, D. Laera, T. Poinsot, T. Schuller, and L. Selle. 2025. Analysis of the origin of NOx emissions in non-premixed dual swirl hydrogen flames. *Combust. Flame* 273:113925.
[14] Vaysse, N., D. Durox, R. Vicquelin, S. Candel, and A. Renaud. 2023. Stabilization and dynamics of pure hydrogen swirling flames using cross-flow injection. *Proc. ASME Turbo Expo* 3A–2023:1–12.
[15] Leroy, M., C. Mirat, A. Renaud, S. Puggelli, S. Zurbach, and R. Vicquelin. 2024. Structure and NOx emissions of stratified hydrogen-air flames stabilized on a coaxial injector. *J. Eng. Gas Turbines Power* 146.
[16] Leroy, M., S. Puggelli, C. Mirat, A. Renaud, J. Leparoux, Q. Buisson, R. Mercier, and R. Vicquelin. 2024. Investigation of NOx scaling laws in swirled partially premixed hydrogen flames on a coaxial injector. *Int. J. Hydrogen Energy* 91:256–66.
[17] Paniez, H., S. Marragou, H. Magnes, and T. Schuller. 2024. High-frequency thermo-acoustic instability in a dual swirl H_2 burner. *Proc. Combust. Inst.* 40:105679.
[18] Cozzi, F., F. Motta, F. Cobianchi, L. Zampini, and A. Francabandiera. 2019. Experimental analysis of a double swirl burner. *42nd Meeting of the Italian Section of the Combustion Institute* (Ravenna):1–6.
[19] Pirci, A. 2020. Unconfined NG/H_2 flame stability and flame morphology analysis in a double swirl burner. MSc thesis. *Politecnico di Milano*.
[20] Iapaolo, F., and F. Cozzi. 2025. Experimental investigation of the isothermal flow field in an air staged multiswirl 100% hydrogen burner. *J. Phys. Conf. Ser.* (accepted).
[21] Kalantari, A., and V. McDonell. 2017. Boundary layer flashback of non-swirling premixed flames: mechanisms, fundamental research, and recent advances. *Prog. Energy Combust. Sci.* 61:249–92.
[22] Liu, X., and Q. Zhang 2014. Influence of initial pressure and temperature on flammability limits of hydrogen–air. *Int. J. Hydrogen Energy* 39:6774–82.
[23] Schefer, R. W., W. D. Kulatilaka, B. D. Patterson, and T. B. Settersten. 2009. Visible emission of hydrogen flames. *Combust. Flame* 156:1234–41.
[24] Iapaolo, F., F. Cozzi, E. Ciuffoli, and P. Rocco. 2025. Experimental characterization of emissions and flame morphology of a partially-premixed dual-swirl 100% hydrogen burner. *European Combustion Meeting (ECM 2025)*.